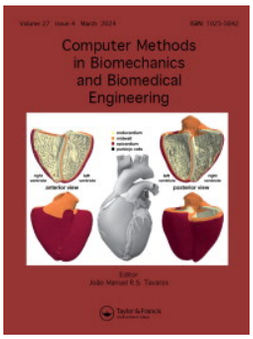

Computer Methods in Biomechanics and Biomedical Engineering

ISSN: (Print) (Online) Journal homepage: www.tandfonline.com/journals/gcmb20

Effects of cardiac growth on electrical dyssynchrony in the single ventricle patient

O. Z. Tikenoğulları, M. Peirlinck, H. Chubb, A. M. Dubin, E. Kuhl & A. L. Marsden

To cite this article: O. Z. Tikenoğulları, M. Peirlinck, H. Chubb, A. M. Dubin, E. Kuhl & A. L. Marsden (14 Jun 2023): Effects of cardiac growth on electrical dyssynchrony in the single ventricle patient, Computer Methods in Biomechanics and Biomedical Engineering, DOI: 10.1080/10255842.2023.2222203

To link to this article: https://doi.org/10.1080/10255842.2023.2222203

Published online: 14 Jun 2023.

Submit your article to this journal

Article views: 290

View related articles

View Crossmark data

Citing articles: 1 View citing articles

Full Terms & Conditions of access and use can be found at
https://www.tandfonline.com/action/journalInformation?journalCode=gcmb20

COMPUTER METHODS IN BIOMECHANICS AND BIOMEDICAL ENGINEERING
https://doi.org/10.1080/10255842.2023.2222203

Taylor & Francis
Taylor & Francis Group

Check for updates

Effects of cardiac growth on electrical dyssynchrony in the single ventricle patient

O. Z. Tikenoğulları[a], M. Peirlinck[b], H. Chubb[c], A. M. Dubin[c], E. Kuhl[a] and A. L. Marsden[a,c,d,e]

[a]Department of Mechanical Engineering, Stanford University, Stanford, CA, USA; [b]Department of Biomechanical Engineering, Delft University of Technology, Delft, Netherlands; [c]Department of Pediatrics (Cardiology), Stanford University, Stanford, CA, USA; [d]Department of Bioengineering, Stanford University, Stanford, CA, USA; [e]Institute for Computational and Mathematical Engineering, Stanford University, Stanford, CA, USA

ABSTRACT

Single ventricle patients, including those with hypoplastic left heart syndrome (HLHS), typically undergo three palliative heart surgeries culminating in the Fontan procedure. HLHS is associated with high rates of morbidity and mortality, and many patients develop arrhythmias, electrical dyssynchrony, and eventually ventricular failure. However, the correlation between ventricular enlargement and electrical dysfunction in HLHS physiology remains poorly understood. Here we characterize the relationship between growth and electrophysiology in HLHS using computational modeling. We integrate a personalized finite element model, a volumetric growth model, and a personalized electrophysiology model to perform controlled in silico experiments. We show that right ventricle enlargement negatively affects QRS duration and interventricular dyssynchrony. Conversely, left ventricle enlargement can partially compensate for this dyssynchrony. These findings have potential implications on our understanding of the origins of electrical dyssynchrony and, ultimately, the treatment of HLHS patients.

ARTICLE HISTORY
Received 26 October 2022
Accepted 4 May 2023

KEYWORDS
Hypoplastic left heart syndrome; congenital heart disease; cardiac electrophysiology; growth and remodeling; dyssynchrony

1. Introduction

Hypoplastic left heart syndrome (HLHS) is a severe congenital cardiac defect where the left ventricle is underdeveloped and the systemic outflow tract is obstructed (Noonan and Nadas 1958). HLHS occurs in 1.8 of 10,000 live births and represents 3.8% of all patients suffering from congenital heart disease (Ferencz et al. 1985). Without intervention, HLHS is uniformly fatal. Having drastically improved over the past four decades, the current treatment for HLHS – and other functional single right ventricle lesions – involves a series of two (hybrid approach) or three (traditional approach) palliative surgical procedures that establish the Fontan circulation (Fontan and Baudet 1971). In the resulting physiology, the right ventricle is established as the sole ventricular pumping chamber that propels blood through both the systemic and the pulmonary circulations and the venous return is routed directly to the pulmonary arteries. Regardless of the approach, longitudinal data from birth show that only two thirds of the patients born with HLHS today may hope to reach adulthood (Ohye et al. 2016).

Despite improved mortality rates, the series of surgeries that create the Fontan physiology in HLHS patients is not curative and exposes the right ventricle to a systemic workload it is not built for (Files and Arya 2018). HLHS patients can develop a number of sequelae in the years following the Fontan procedure, including heart failure, arrhythmia, protein losing enteropathy, coagulopathy, exercise intolerance, portal hypertension, and lymphatic dysfunction. Over time, growth and remodeling in the single ventricle often leads to ventricular enlargement (Sobh et al. 2022) and a prolongation of the QRS segment in the electrocardiogram (Graham et al. 2007; Tsai et al. 2013). Both aspects are correlated with ventricular dyssynchrony, which frequently accelerates the development of heart failure (Rösner et al. 2018; Zaidi et al. 2019). Once the single ventricle begins to fail, heart transplantation, accompanied by associated consequences of immune suppression, or mechanical circulatory support are often the only viable options for the patient to survive (Gutgesell and Massaro 1995; Lopez et al. 2010; Rathod et al. 2014).

In adult patients with normal anatomy and ventricular dyssynchrony, cardiac resynchronization

CONTACT A. L. Marsden amarsden@stanford.edu
© 2023 Informa UK Limited, trading as Taylor & Francis Group

therapy is a well-established treatment modality. However, the use of cardiac resynchronization therapy in pediatric and congenital heart disease patients is less established (Joyce et al. 2020). For single ventricle patients specifically, no study has been able to demonstrate a significant improvement in survival (Chubb et al. 2022). Furthermore, the risk of transplantation or death has been shown to be up to four times higher in paced versus non-paced HLHS patient cohorts (Chubb et al. 2022). This substantially raised hazard ratio is thought to be correlated with the discoordinated contraction of the paced single ventricle. However, these dyssynchrony mechanisms in the single ventricle patient populations remain poorly understood (Motonaga et al. 2012). Therefore, an improved understanding of the electrophysiology of the single ventricle heart is urgently required to improve ventricular pacing and cardiac resynchronization therapies in this high risk patient population.

The lack of established single ventricle animal models (Wünnemann and Andelfinger 2016) and the small yet highly heterogeneous single ventricle patient population make it highly challenging to infer insights from (pre)clinical data into single ventricle function and dysfunction. Therefore, we turn to biophysical cardiac computational modeling to provide a mechanistic understanding of the onset and progression of electrical dyssynchrony in the single ventricle patient. More specifically, we design and calibrate a personalized image-based cardiac anatomic model from an HLHS patient and perform electrophysiological simulations. Using this model, we explore how right and left ventricular overload induces growth, and how this growth induces electrical dyssynchrony in this single ventricle patient.

2. Materials and methods

To design a personalized heart model, we obtained medical images and electrocardiographic data from a six-and-a-half-year-old HLHS patient. We segmented the cardiac geometry to create a personalized finite element model and incorporated rule-based Purkinje and myocardial fiber architectures for electrophysiological simulations. We extracted electrocardiogram readings and calculated personalized activation times to characterize electrical dyssynchrony. We then investigated the effect of loading-induced growth on electrical dyssynchrony by simulating kinematic growth following pressure-induced inflation of the right and left ventricles. We used modified numerical quadrature rules to minimize the mesh sensitivity of our simulated conduction velocities. We preserved the original Purkinje and myocardial fiber architectures by mapping them from the baseline geometry to the grown geometries. We simulated the electrical dyssynchrony in the grown and remodeled states using the earlier obtained personalized electrophysiology parameters and compared these results to follow-up electrocardiogram recordings. The following sections describe the steps of our modeling pipeline in more detail.

2.1. Personalized finite element model

This study focuses on a six-and-a-half-year-old female with a hypoplastic left ventricle who had undergone the Fontan procedure at age two. We obtained medical imaging and electrocardiographic data for this patient under an IRB approved protocol. We segmented the biventricular geometry from magnetic resonance images using the Simvascular software (Updegrove et al. 2017), and converted the resulting geometry with a cutoff at the base plane, 5 mm above mitral and tricuspid valves, into a 611,864 tetrahedral element mesh using Gmsh software (Geuzaine and Remacle 2009) (see Figure 1, left). We used linear element formulation in electrophysiology simulations. However, in order to prevent locking of linear tetrahedral elements, we used quadratic element formulation with reduced integration rule in simulating growth mechanics.

The His-Purkinje system is a network of fast-conducting cells that forms an integral part of the cardiac excitation system. We created the Purkinje network for both ventricles using a fractal tree and projection algorithm proposed by Costabal et al. (2016). We initiated the left and right Purkinje networks from the endocardial locations near the atrioventricular node and constrained these networks to stay approximately 10 mm below the base plane. Parameters of the fractal tree algorithm we used to generate left and right Purkinje networks are given in Table 1. The resulting dense networks consists of 53,642 line elements in total, with an average element size of 0.16 mm. Both fiber networks have 3343 end-points in total, with 280 in left and 2863 in left endocardium, where the Purkinje-myocardium junctions are established. An algorithm we developed for this purpose iterates through the Purkinje end-nodes and for each Purkinje end-node finds the closest myocardium node in order to create a Purkinje-myocardium junction. When an end-node is paired to a myocardium node, the algorithm assigns the number and the coordinate

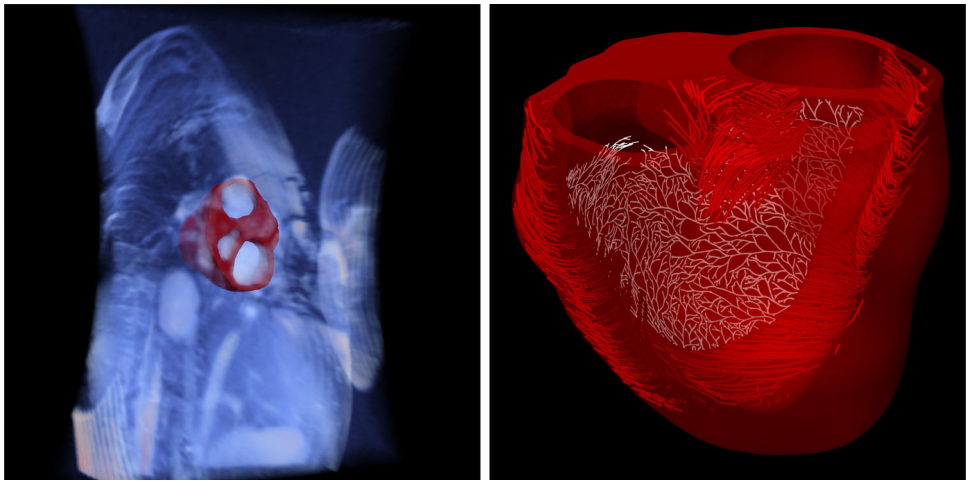

Figure 1. Biventricular geometry of the heart generated from magnetic resonance images of a 6.5-year-old hypoplastic left heart syndrome patient using the Simvascular software (left). Heart model discretized with 611,864 tetrahedral elements with individual myofiber orientations and Purkinje network discretized with 53,642 line elements (right).

Table 1. Parameters of the fractal tree algorithm (Costabal et al. 2016), used for generating left and right Purkinje networks.

Parameter name		Left Purkinje		Right Purkinje	
init_length	N_it	7.0	20	20.0	40
length	std_length	1.0	$\sqrt{0.2}\times$ length	1.5	$\sqrt{0.2}\times$ length
min_length	branch_angle	length /10.0	0.2	length/10.0	0.2
w	l_segment	0.15	0.1	0.15	0.15
Fascicles	Fascicles_angles	True	[0.5, − 0.5]	True	[1.5, − 1.5, 0.0]
Fascicles_length		[3.0, 3.0]		[7.0, 7.0, 7.0]	

values from the myocardium node to the Purkinje end-node, virtually making them the same node, therefore the transmembrane potentials are identical. In this way, Purkinje-myocardium junction becomes established, allowing the electrical signal transmission from the Purkinje network to the myocardium mesh. Left and right networks are not connected to each other and need to be activated by independent electrical stimuli (see Figure 1, right).

In addition to the Purkinje system, the anisotropic structure of the myocardium plays an important role in the spatiotemporal excitation of the heart. We assign transmurally varying fiber orientations to our computational heart model using the Laplace-Dirichlet rule-based approach Bayer et al. (2012). In line with *ex vivo* DTMRI experiments of human heart tissue (Rohmer et al. 2007), we assign a transmural fiber orientation ranging from $+40°$on the endocardium to $-50°$on the epicardium for both ventricles (see Figure 1, right).

2.2. Electrophysiology modeling

We simulated the spatiotemporal evolution of the transmembrane potential V across the heart using the mono-domain electrophysiology equation,

$$\chi\ (c\dot{V} + I_{\text{ion}}\ ) - \text{div}(\mathbf{D}\cdot\nabla V) = I_{\text{stim}}. \qquad (1)$$

Here, χ is the surface-to-volume ratio, c is the capacitance of the cell membrane, and $\mathbf{D}$ is the anisotropic conductivity tensor. I_{ion} is the ionic current generated by ion transport across the cell membrane and I_{stim} is the external stimulus. We applied an external stimulus of $I_{\text{stim}} = 50\ \mu A/\text{mm}^3$ for a duration of 2 ms to the initial nodes of the right and left Purkinje networks at times $t = t^{RV}_{\text{stim}}$ and $t = t^{LV}_{\text{stim}}$, which we determined through the personalization of the electrophysiology model (see, Section 2.3). The ionic current I_{ion} is a function of the transmembrane potential V and a set of state variables of the underlying ionic model. In simulations we used a dedicated ionic model for the Purkinje fiber cells proposed in Ten Tusscher and Panfilov (2008) and a dedicated ionic model for ventricular cardiomyocytes proposed in Ten Tusscher and Panfilov (2006). In our electrophysiology model we did not distinguish the ionic model differences between endocardial, mid-myocardial and epicardial layers. We used endocardial variant of the Ten Tusscher-Panfilov model (Ten Tusscher and Panfilov 2006) for all myocardium cells. We note that some recent ionic models have advanced the Ten Tusscher-Panfilov model, for

example O'Hara-Virág-Varró-Rudy model (O'Hara et al. 2011) is shown to be able to model early afterdepolarizations where Ten Tusscher-Panfilov model fails. However, the improved modeling accuracy comes with an elevated computational cost: O'Hara-Virág-Varró-Rudy model employs 41 state variables which is significantly more than the 18 state variables used by the Ten Tusscher-Panfilov model. We do not simulate complex electrophysiological processes in this study, therefore we contented our simulations with the Ten Tusscher-Panfilov model in order to keep the computational cost tractable. With no-flux boundary conditions, the weak form of Equation (1) becomes

$$\int_{\mathcal{B}} \chi \; c\dot{V} \;\; \delta V + \nabla V \cdot \mathbf{D} \cdot \nabla \delta V + \chi \;\; I_{\text{ion}} \delta V - I_{\text{stim}} \delta V \; \mathrm{d}v = 0, \tag{2}$$

for all admissible test functions δV. We obtain the matrix form of the electrophysiology equation by applying a finite element discretization to the weak form in Equation (2) and split the matrix form into ionic and diffusion parts (Qu and Garfinkel 1999; Krishnamoorthi et al. 2013),

$$\mathbf{C}_1 \cdot \dot{\mathbf{V}} + \mathbf{D} \cdot \mathbf{V} = \mathbf{0} \;\; (\text{diffusion}) \qquad \mathbf{C}_2 \cdot \dot{\mathbf{V}} + \mathbf{M} \cdot \mathbf{I}_{\text{ion}} = \mathbf{0} \;\; (\text{ionic}), \tag{3}$$

where $\mathbf{C}_1$ and $\mathbf{C}_2$ are the capacitance matrices, $\mathbf{D}$ is the conductance matrix, $\mathbf{M}$ is the mass matrix, $\mathbf{I}_{\text{ion}}$ is the transmembrane current vector, and $\mathbf{V}$ is the transmembrane potential vector. To calculate the matrices $\mathbf{C}_1$ and $\mathbf{D}$, we used a modified four-point quadrature rule in the tetrahedral elements and a modified two-point quadrature rule in the line elements (Pezzuto et al. 2016; Woodworth et al. 2022). Each quadrature point has equal weight in a given quadrature rule, however we modify the location of these points as explained in Section 2.6. In doing so, we position each quadrature point along a line that runs from the element centroid to a vertex, which is illustrated for a sample quadrature point in Figure 2. As a result, each quadrature point in a given quadrature rule is at equal distance from the centroid, however in different directions. In the ionic part of problem, we applied matrix lumping and obtained two diagonalized matrices $\mathbf{C}_2$ and $\mathbf{M}$ as described in Krishnamoorthi et al. (2013). This approach is equivalent to using nodal integrations in calculating the matrices. Therefore, we store the gating variables of the ionic model at the nodes and run the ionic updates strictly at the nodes. We integrated the diffusion equations in time using the Backward-Euler method with a uniform time step size of 0.10 ms and the ionic equations using a fourth-order Runge-Kutta method with a uniform time step size of 0.05 ms.

To couple the Purkinje system to the excitable myocardial tissue, we connected the end-points of the Purkinje network to the myocardium directly, as described in Section 2.2. At the Purkinje-myocardium junction nodes, we performed ionic updates using the myocardial ionic model. We solved the resulting electrophysiology problem using the finite elements method as described in Krishnamoorthi et al. (2013). See Appendix A for the validation of our electrophysiology solver.

To parameterize our model, we started with the ionic model parameters for human Purkinje fiber cells (Ten Tusscher and Panfilov 2008) and ventricular cardiomyocytes (Ten Tusscher and Panfilov 2006) and with anisotropic conductivity values for the conductivity tensor $\mathbf{D}$ (Niederer et al. 2011). We further personalized the model based on electrocardiographic recordings as described in Section 2.3. After solving the electrophysiology model (Equation (3)), we computed virtual electrocardiogram recordings from the computed spatiotemporal transmembrane potential evolution. Specifically, we calculated the pseudo-electrocardiographic signal ϕ_e by integrating the directional multiplication of the gradient of transmembrane potential at each point in the cardiac domain with the direction vector pointing from the integration location to a lead location $\mathbf{x}_e$ (Sahli Costabal et al. 2018),

$$\phi_e(\mathbf{x}_e) = -\int_{\mathcal{B}} \nabla V \cdot \nabla (1/||\mathbf{r}||) \; \mathrm{d}v, \tag{4}$$

where $\mathbf{r}$ is the direction vector from the point within the heart model $\mathcal{B}$ to the virtual lead position. To correctly locate the virtual leads, we estimated the coordinates $\mathbf{x}_e$ using the magnetic resonance imaging scan (Figure 1) for three electrocardiogram leads $e = \{\text{V2}, \text{V6}, \text{AVF}\}$.

2.3. Personalization of electrophysiology parameters

After constructing the electrophysiological finite element model, we calibrated our electrophysiology model parameters to approximate the clinical electrocardiogram recordings of our HLHS patient. In developing the procedure for parameter calibration, we adopted a methodology similar to the one proposed in Gillette et al. (2018), by optimizing stimulus timing and

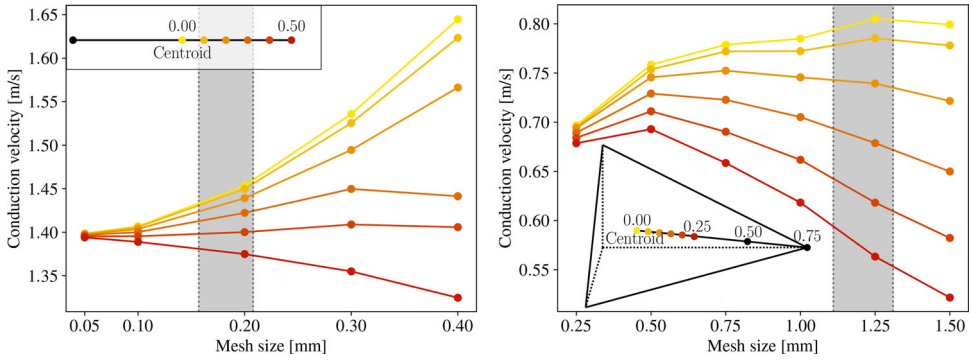

Figure 2. Change in conduction velocities with mesh size, for different quadrature point locations. Conduction velocities are plotted in the range $[0.00, 0.50]$ for line elements and $[0.00, 0.25]$ for tetrahedral elements, where Gauss quadrature locations correspond to 0.21 and 0.34. Shaded gray regions represent the average element sizes in our baseline and grown heart models. To minimize the mesh sensitivity of conduction velocities within the gray region, we selected quadrature point locations of 0.40 for line elements and 0.05 for tetrahedral elements.

conduction velocities. However, we used monodomain finite element solver instead of reaction-Eikonal solving method, and we used a bespoke Purkinje network instead of applying stimuli directly to myocardium. In our study, we optimized the conductivities $\mathbf{D}$ of the Purkinje network and the myocardium tissue independently, and we optimized the timing of the external stimulus applied to each Purkinje networks, t^{RV}_{stim} and t^{LV}_{stim} such that our spatiotemporal activation patterns match the electrocardiogram recordings of leads V2, V6, and AVF. Resulting parameters at the end of optimization are given in Section 3.1. We used the data from V2, V6, and AVF leads of the clinical ECG recordings, in calibration of the personalized electrophysiology parameters. Our reason to choose these three ECG leads is to inform our personalization procedure of three dimensional electrical activity. Specifically; V2 lead is positioned on the chest and measures the electrical activity in anterior-posterior axis, V6 lead is positioned near the armpit and measures electrical activity in medial-lateral axis, AVF lead attached to the left leg and measures electrical activity in inferior-superior axis. The combination of these three axes gives us sufficient three-dimensional insights in the spatiotemporal activation sequence of the heart to calibrate the personalized electrophysiology model. Starting from the initial parameter values of Section 2.1, we performed a parameter search using the Nelder-Mead optimization algorithm in order to tune the electrophysiology model parameters to match the patient specific electrocardiogram (Virtanen et al. 2020). We defined the objective function as the root mean square error of the simulated and measured electrocardiogram signals,

$$\text{err} = \sum_{e} \frac{1}{n} \left(\sum_{i=1}^{n} (\phi^{\text{sim}}_{e,i} - \phi^{\text{dat}}_{e,i})^2 \right)^{1/2} \quad \text{for} \quad e = \{\text{V2}, \text{V6}, \text{AVF}\} \ , \tag{5}$$

where $\phi^{\text{sim}}_{e,i}$ and $\phi^{\text{dat}}_{e,i}$ are the simulated and measured electrocardiogram readings and n is the number of data points in time. As the stopping criteria of the parameter search process, we used the function value tolerance option `fatol` in SciPy's Nelder-Mead implementation. We have set $\texttt{fatol} = 1 \times 10^{-3}$. Each electrophysiology simulation took about one hour to complete on a high performance computing (HPC) cluster using 24 cores of Intel 5118 CPUs. The complete optimization process took about 75 function evaluations, requiring about three days of wall-clock time.

2.4. Dyssynchrony measures

To quantify the electrical performance we used two measures of electrical dyssynchrony, the electric activation time and the electric dyssynchrony index (Motonaga et al. 2012). The electrical activation time t^{eat}_i of each ventricle $i = \{\text{RV}, \text{LV}\}$ is the difference between the latest and earliest local electrical activation times, $\max(t^{\text{act}}_{j,i})$ and $\min(t^{\text{act}}_{j,i})$, where $t^{\text{act}}_{j,i}$ is an array that contains the time values at which the transmembrane potential of all $j = 1, \ldots, n$ endocardial points became positive,

$$t^{\text{eat}}_i = \max(t^{\text{act}}_{j,i}) - \min(t^{\text{act}}_{j,i}) \quad \text{for} \quad i = \{\text{RV}, \text{LV}\} \ . \tag{6}$$

The electrical dyssynchrony index t^{dys}_i of each ventricle $i = \{\text{RV}, \text{LV}\}$ is the standard deviation of the

local activation times $t_{j,i}^{\mathrm{act}}$ from the mean ventricular activation time μ_i,

$$t_i^{\mathrm{dys}} = \frac{1}{n}\sum_{j=1}^{n}(t_{i,j}^{\mathrm{act}} - \mu_i) \quad \text{with}$$
$$\mu_i = \frac{1}{n}\sum_{j=1}^{n} t_{i,j}^{\mathrm{act}} \quad \text{for} \quad i = \{\mathrm{RV}, \mathrm{LV}\}\ . \tag{7}$$

The interventricular dyssynchrony is the difference between the mean activation times of the left and right endocardial surfaces, $\mu_{\mathrm{LV}} - \mu_{\mathrm{RV}}$.

2.5. Kinematic-based growth modeling

We model the growth of the heart using a kinematic growth model (Göktepe et al. 2010a). We assume a kinematic decomposition of the deformation gradient $\mathbf{F}$ into elastic and growth parts,

$$\mathbf{F} = \mathbf{F}^{\mathrm{e}} \cdot \mathbf{F}^{\mathrm{g}}\ , \tag{8}$$

where $\mathbf{F}^{\mathrm{g}}$ describes the spin-free growth tensor that maps tangent elements from the undeformed configuration to an incompatible intermediate configuration and $\mathbf{F}^{\mathrm{e}}$ is the elastic tensor restores the compatibility of the full deformation gradient $\mathbf{F}$. To model the growth of the heart as a result of a chronic ventricular overload, we define the evolution of the second order growth tensor $\mathbf{F}^{\mathrm{g}}$ in response to mechanical loading. Here we adopt a stretch-driven growth model in which isotropic growth is driven by the elastic overstretch of the muscle fibers. This implies that the growth tensor $\mathbf{F}^{\mathrm{g}}$ takes a diagonal format and the growth factor ϑ is a function of the elastic stretch λ^{e} in the fiber direction,

$$\mathbf{F}^{\mathrm{g}} = \vartheta^{1/3}\ \mathbf{I} \qquad \text{with} \qquad \dot{\vartheta} = \frac{1}{\tau}[\ \lambda^{\mathrm{e}} - 1\ ]. \tag{9}$$

The parameter τ governs the growth rate, but is not relevant in our simulations because here we are only interested in the steady state of the growth model at different stages, as the time scale is much longer compared with electrophysiological simulations. Our biventricular geometry was built based on end-diastolic images and we take λ^{e} as the relative stretch state at this end-diastolic stage. Therefore any stretch beyond this state causes growth through $\lambda^{\mathrm{e}} > 1$. At the steady state of the growth simulations, elastic fiber stress relaxes completely and the fibers reach an unstressed state. At this point elastic component of the fiber stretch recovers its initial value $\lambda^{\mathrm{e}} = 1$. To model the elastic response of myocardial tissue, we incorporate its hyperelastic, anisotropic, and nearly incompressible tissue behavior (Sommer et al. 2015; McEvoy et al. 2018) using the following strain energy function (Holzapfel and Ogden 2009),

$$\begin{aligned}\Psi = {} & \frac{a}{2b}\exp\left(b[\bar{I}_1^{\mathrm{e}} - 3]\right) + \frac{a_{\mathrm{f}}}{2b_{\mathrm{f}}}\left[\exp\left(b_{\mathrm{f}}[\bar{I}_{4\mathrm{f}}^{\mathrm{e}} - 1]^2\right) - 1\right] \\ & + \frac{a_{\mathrm{s}}}{2b_{\mathrm{s}}}\left[\exp\left(b_{\mathrm{s}}[\bar{I}_{4\mathrm{s}}^{\mathrm{e}} - 1]^2\right) - 1\right] \\ & + \frac{a_{\mathrm{fs}}}{2b_{\mathrm{fs}}}\left[\exp\left(b_{\mathrm{fs}}[\bar{I}_{8\mathrm{fs}}^{\mathrm{e}} - 1]^2\right) - 1\right] \\ & + \frac{1}{4}\kappa[J^2 - 1]\ln(J).\end{aligned} \tag{10}$$

Here, invariants of deformation are defined as

$$\begin{aligned}&\bar{\mathbf{C}}^{\mathrm{e}} = J^{-2/3}\mathbf{F}^{\mathrm{et}} \cdot \mathbf{F}^{\mathrm{e}} \quad \bar{I}_{4\mathrm{f}}^{\mathrm{e}} = \bar{\mathbf{C}}^{\mathrm{e}} : \mathbf{f}_0 \otimes \mathbf{f}_0 \quad J = \det(\mathbf{C})^{1/2} \\ &\bar{I}_1^{\mathrm{e}} = \bar{\mathbf{C}}^{\mathrm{e}} : \mathbf{I} \quad \bar{I}_{4\mathrm{s}}^{\mathrm{e}} = \bar{\mathbf{C}}^{\mathrm{e}} : \mathbf{s}_0 \otimes \mathbf{s}_0 \quad \bar{I}_{8\mathrm{fs}}^{\mathrm{e}} = \mathrm{sym}(\bar{\mathbf{C}}^{\mathrm{e}} : \mathbf{f}_0 \otimes \mathbf{s}_0),\end{aligned} \tag{11}$$

where $\mathbf{F}$ is the deformation gradient, κ is the bulk modulus, and $a, a_{\mathrm{f}}, a_{\mathrm{s}}, a_{\mathrm{fs}}, b, b_{\mathrm{f}}, b_{\mathrm{s}}, b_{\mathrm{fs}}$ are the material parameters that govern the anisotropic response of the tissue. We note that the elastic deformation is volume-preserving (incompressible), however the overall deformation including the growth part is not volume-preserving. We took the constitutive model parameters from the study of (Peirlinck et al. 2019b), where authors calibrated parameters based on diastolic filling simulations and Klotz-relation (Klotz et al. 2006). In addition, we applied realistic kinematic boundary conditions to constrain our finite element model in space. We used a continuum distributed coupling approach to constrain the left ventricular annulus nodes with respect to the fixed center of mass of the annulus and fixed the out-of-plane motion of the nodes on the base cut plane.

We simulated homeostatic growth in response to a ventricular pressure of 10 mmHg. We applied this pressure in three different scenarios: We pressurized both ventricles, only the right ventricle, and only the left ventricle and refer to the simulations as RV + LV, RV, and LV throughout the remainder of this study. For all growth simulations, we adopted a custom designed kinematic growth-based user subroutine (Peirlinck et al. 2019a) within the commercial finite element software Abaqus (Dassault Systèmes Simulia Corp 2022). We performed all growth simulations in Abaqus/Explicit using automatic time stepping with a minimum time interval of 10^{-6} s.

2.6. Mesh sensitivity of conduction velocities

Growth deforms the finite element model of the heart and alters the mesh size in comparison to the baseline geometry. Changing the mesh size changes the

simulated conduction velocity because coarse meshes tend to either under- or over-estimate the conduction velocities depending on the quadrature method used (Krishnamoorthi et al. 2013). To ensure consistency of results, it is necessary to minimize the change in simulated conduction velocities due to change in mesh size. Previous studies proposed a method to minimize the error in conduction velocities by using non-Gaussian quadrature strategies (Pezzuto et al. 2016; Woodworth et al. 2022). Here we adapt the same approach however we choose the non-Gaussian quadrature points such that the simulated conduction velocities are less sensitive to change in mesh size.

Figure 2 shows the simulated conduction velocities with respect to the mesh size for different locations of non-Gaussian quadrature points (those are marked on the representative line and tetrahedral elements). We calculated that the average size of Purkinje line elements is 0.16 mm before growth and size increased up to 0.21 mm after growth. Similarly, average edge size of tetrahedral elements increased from 1.11 mm up to 1.31 mm in myocardium mesh. These ranges are marked with gray vertical regions in Figure 2. Our goal is to have a minimal change in simulated conduction velocities, within the aforementioned ranges of mesh sizes. Therefore, we proceed to identify the most horizontal line in each plot, within the gray regions, that represents the least change in conduction velocity. The quadrature location corresponding to the chosen line is selected to be the optimal quadrature location for our electrophysiology model. Using this reasoning, we selected quadrature locations 0.40 for line elements (Figure 2, left) and 0.05 for tetrahedral elements (Figure 2, right) as optimal quadrature locations, because these lines show the least amount of variability (more horizontal) within the gray regions. We use these optimal quadrature locations only for solving the diffusion part of the electrophysiology problem in Equation (3), whereas for the ionic part of the problem we use nodal quadratures.

3. Results

3.1. Personalized electrophysiology model

At the end of the personalization process, we obtained the optimized parameters as follows: conductivity tensor for myocardium $\mathbf{D}_{\text{myo}} = (1.05 \times 10^{-3})\mathbf{I} + (6.95 \times 10^{-3})\mathbf{f}_0 \otimes \mathbf{f}_0$ [S mm^{-1}]; conductivity tensor for Purkinje $\mathbf{D}_{\text{pur}} = (1.26 \times 10^{-2})\mathbf{I}$ [S mm^{-1}]; stimulus timing of right Purkinje $t^{RV}_{\text{stim}} = 145$ ms; stimulus timing of left Purkinje $t^{RV}_{\text{stim}} = 165$ ms. Simulated electrocardiogram recordings resulting from the optimized parameters are given in Figure 3.

Table 2 summarizes the resulting conduction velocities for the His-Purkinje network and the myocardial tissue, the electrical activation times, and the dyssynchrony indices according to Section 2.4, as a result of the personalized electrophysiology model.

3.2. Growth of personalized geometry

Figure 4 illustrates the baseline and grown geometries of three loading-induced scenarios. The sections highlight the enlargement of the heart and the growth-induced residual fiber stretch in the ventricular muscle tissue. Table 3 summarizes the growth-induced volume changes. For the RV + LV case, we observe that the left ventricular cavity enlarged by 47% whereas the right ventricular cavity enlarged by 101%, indicating that the left ventricle is stiffer and less sensitive to pressure-induced growth. Compared to the clinical catheterization laboratory reports, the patient's right ventricular volume grew from 38.0 mL to 75.1 mL from age 6 years and 6 months to age 11 years and 4 months. The right ventricular enlargement predicted by our RV + LV growth model corresponded to roughly six years of age difference in the patient's life. Left ventricular loading alone resulted in a 56% and 4% increase of the left and right ventricular volumes; right ventricular loading resulted in a 37% and 99% enlargement.

3.3. Growth-induced changes in electrocardiogram readings

Figure 5 illustrates our simulated baseline electrocardiogram readings and the predicted electrocardiogram readings for our grown hypoplastic left heart syndrome models using the personalized electrophysiology parameters from Section 3.1. We showcase the growth-induced changes in these electrocardiograms for ten 10% growth increments with respect to the final grown configurations from Section 3.2. From our results, we conclude that RV-only and RV + LV load-induced growth cause an increase in the amplitude and length of the QRS complex and the T wave. At the same time, LV-only loaded growth causes smaller changes in the electrocardiogram readings. More specifically, the QRS duration increased about 20 ms for RV and RV + LV load-induced growth and about 2 ms for LV load-induced growth.

3.4. Interventricular dyssynchrony

Figure 6 illustrates the distribution of local electrical activation times t^{act} (see, Section 2.4) of the left and

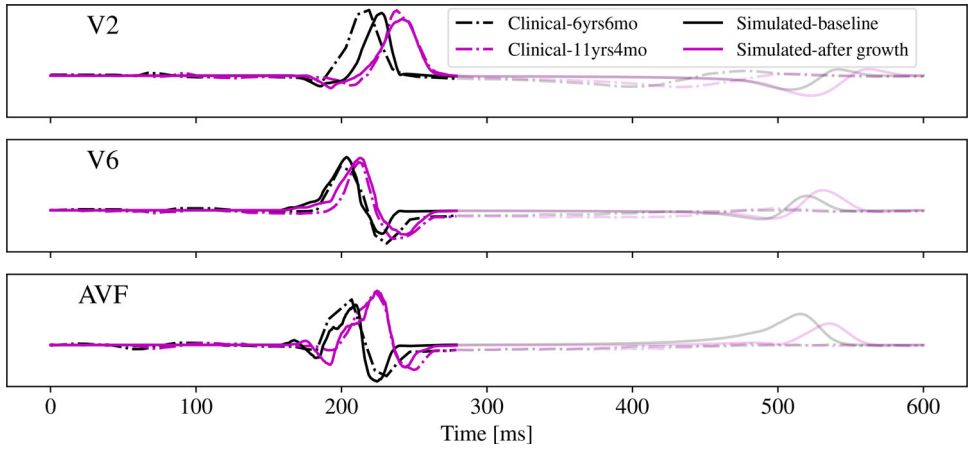

Figure 3. Clinical electrocardiogram recording of the patient is compared to the simulated electrocardiograms. Black lines represent the electrocardiograms before growth, and magenta lines represent the electrocardiograms after growth. Simulations of growth are from RV + LV scenario. In the personalization procedure, only the *activation* phase is considered (opaque) and the deactivation phase is omitted (transparent).

Table 2. Conduction velocities and dyssynchrony metrics found from the personalized electrophysiology model agree well with the values reported in literature. Electrophysiology metrics are reported for right ventricle only.

	Conduction velocities		EP metrics	
	Purkinje	Myocardium	Activation time	Dyssync. index
Simulated	1.42m/s	0.78 m/s	68.5 ms	14.7 ms
Literature	1.95m/s[a]	0.70 m/s[a]	63.3 ms[b]	13.7 ms[b]
	2.00 m/s[c]	0.45 m/s[c]		

[a]Barber et al. (2021)
[b]Durrer et al. (1970)
[c]Motonaga et al. (2012)

right ventricle endocardia at baseline and for the three loading-induced growth scenarios. Figure 7 summarizes the growth-induced changes in interventricular dyssynchrony as defined in Section 2.4. In the baseline case, the activation of the right ventricle is slightly delayed compared to the left ventricle. In RV and RV + LV load-induced growth, we observe an increased delay in right ventricular activation, whereas left ventricle activation is delayed to a lesser extent. Expressed more quantitatively, this results in a 7.5 ms and 7.7 ms increase in interventricular dyssynchrony for RV and RV + LV cases as shown in Figure 7. In LV load-induced growth, however, the activation profile of the right ventricle remains almost unaffected, while the activation profile of the left ventricle is shifted to the right. As a result, the activation profiles of the left and right ventricles overlap more and the interventricular dyssynchrony decreases to 1.3 ms.

4. Discussion

During the past four decades, several innovations in the palliative treatment strategy of hypoplastic left heart syndrome have greatly improved survival rates for patients born with this congenital heart defect. Since two-thirds of patients currently have a good chance of making it well into young adulthood (Ohye et al. 2016), it becomes increasingly important to study the long-term morbidities arising in these patients. Despite improved survival rates, many patients with HLHS still face the burden of lifelong complications and remain at high risk of Fontan failure. Up to 50% of all patients with a completed Fontan circulation still require additional interventions before the age of five years Gobergs et al. (2016). The most common follow-up intervention, performed in 8% to 45% of all univentricular patients, is permanent pacemaker implantation. Although unavoidable, ventricular pacing is associated with a 3.8-fold higher risk of transplantation or death (Chubb et al. 2022). As damage induced by ventricular pacing in the single ventricle population is hypothesized to be correlated with a discoordinated contraction of the paced ventricle, we urgently need to improve our understanding of the electromechanical coupling of the single ventricle. This is a challenging endeavor given the high heterogeneity of the single ventricle population and the crescent shape of the right ventricular geometry (Grattan and Mertens 2016; Wen Zhong et al. 2021). Lacking an established single ventricle animal model, we turned to computational modeling to improve our understanding of single ventricle function and dyssynchrony.

Following recent developments in computational modeling, cardiac simulations are increasingly able to replicate the mechanisms of cardiovascular physiology and, as such, deliver more and more opportunities for clinical use (Peirlinck et al. 2021c). Computational models can help to understand the cause of, and

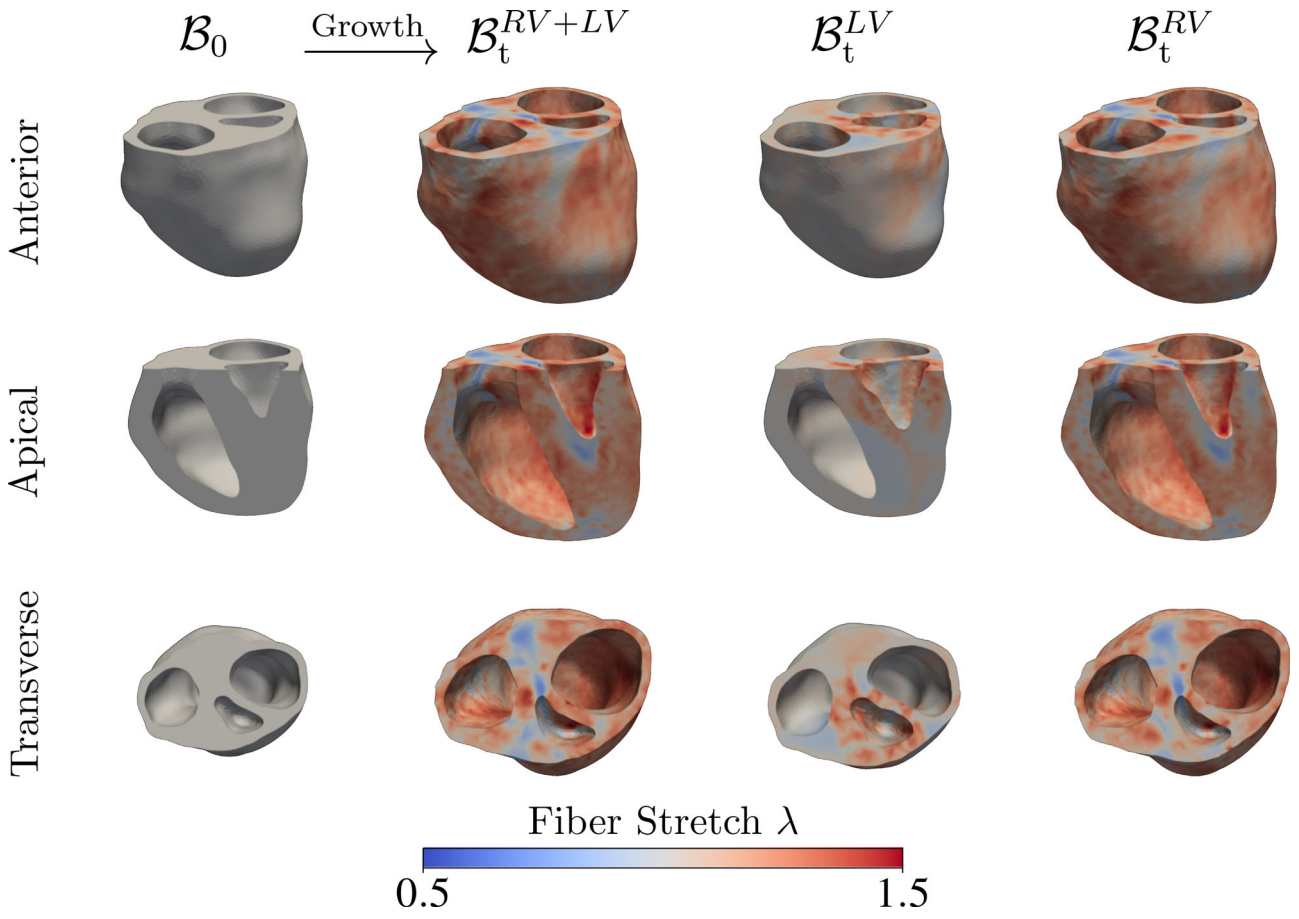

Figure 4. Heart models resulting from the growth simulations. Baseline model and grown models after both right and left ventricular loading, RV + LV, purely left ventricular loading, LV, and purely right ventricular loading, RV, followed by unloading. The fiber stretch λ denotes the total stretch in the myofibers with $\lambda = \vartheta^{1/3}\ \lambda^{e}$. For the LV case, growth is localized around the left ventricle; for the RV and RV + LV cases, growth takes place in both ventricles.

Table 3. Ventricular volumes at the baseline and after growth in response to left and right ventricular loading, RV + LV, purely left ventricular loading, LV, and purely right ventricular loading, RV (upper rows); compared to the right ventricular volume recorded in clinical measurements (lower rows).

	Baseline	RV + LV	LV	RV
Left ventricular volume	1.82 mL	2.67 mL	2.84 mL	2.50 mL
Right ventricular volume	37.98 mL	76.34 mL	39.58 mL	75.52 mL
	age of 6 yrs 6 mo	age of 11 yrs 4 mo		
Right ventricular volume (clinical recording)	38.0 mL	75.1 mL		

improve treatment therapies for, congenital heart defects (Salman and Yalcin 2021; Trusty et al. 2018). In this aspect, lumped parameter network models have become a standard method to study the hemodynamics of congenital heart defects (Marsden and Feinstein 2015), including a.o. the effect of dobutamine in Fontan circulation (Sughimoto et al. 2019) and the performance of total cavopulmonary connection on single ventricle circulation (Sundareswaran et al. 2008). More advanced studies develop personalized coupled three-dimensional computational fluid dynamics models with lumped parameter models, as in Schwarz et al. (2021); Yang et al. (2015) where authors simulated hemodynamics of cavopulmonary grafts. Electrophysiology and growth-and-remodeling of CHDs have received less attention (Lee et al. 2018) and are often modeled with reduced-order lumped parameter network models (Hayama et al. 2020). To the authors' best knowledge, this study is the first attempt to simulate personalized electrophysiology and growth mechanics in single ventricle physiology.

State-of-the-art cardiac electrophysiology and growth modeling approaches in literature allow accurate patient-specific simulations. Cardiac growth and remodeling approaches are summarized in excellent review papers by Sharifi et al. (2021); Niestrawska et al. (2020). We use volumetric growth models and do not consider remodeling in this study. Rodriguez

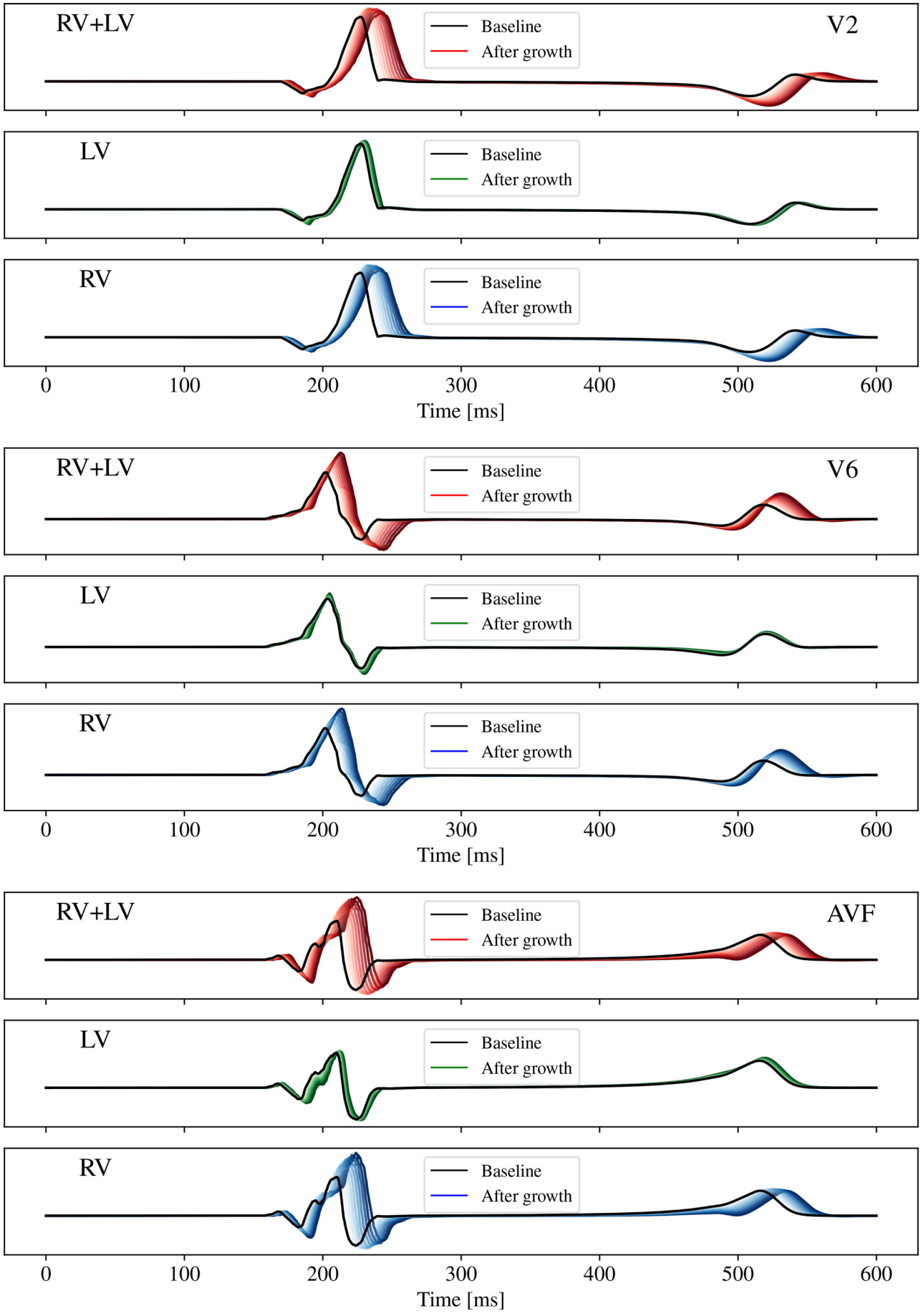

Figure 5. Electrocardiogram readings for baseline and grown geometries in the V2 lead, top, the V6 lead, middle, and the AVF lead, bottom. Baseline electrocardiograms in black and grown heart electrocardiograms in color, interpolated for ten 10% growth increments.

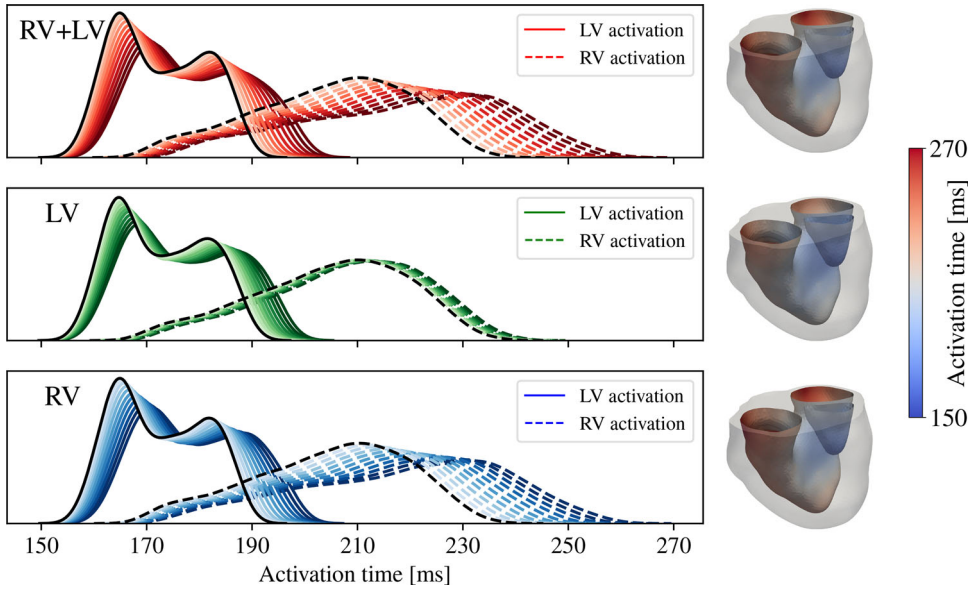

Figure 6. Electrical activation times of baseline and loading-induced growth electrophysiology simulations of the personalized hypoplastic left heart syndrome heart. Solid and dashed black lines highlight the distribution of activation times of the left and right ventricular endocardia at baseline; red, green, and blue lines show the activation times for RV + LV, LV-only, and RV-only load-induced growth. Light to dark colors illustrate the effect of gradual growth, from 10% to 100%, on the activation profiles.

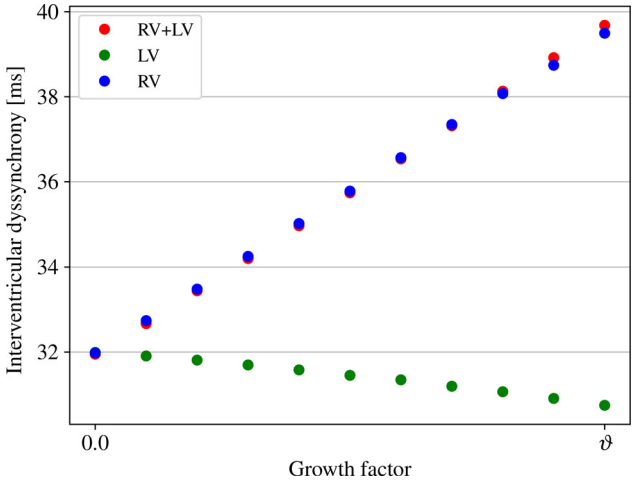

Figure 7. Changes in interventricular dyssynchrony following three scenarios of loading-induced growth. In RV and RV + LV loading-induced growth cases the interventricular dyssynchrony increases from 32.0 ms to 39.5 ms and 39.7 ms, respectively, whereas in the LV loading-induced growth case the interventricular dyssynchrony decreases to 30.7 ms.

et al. (1994) established the foundation of volumetric growth modeling, through the use of multiplicative split of the deformation gradient, in analogy to plasticity. This method was later applied to cardiac growth simulations (Taber and Chabert 2002; Ramasubramanian et al. 2008). Lin and Taber (1995) introduced an evolution law for the growth tensor, and Göktepe et al. (2010b) used stress and strain in the evolution law of growth tensor, therefore linking volumetric growth to biomechanical stimuli . Kroon et al. (2009) applied volumetric growth modeling to a univentricle model, whereas Genet et al. (2016) presented the first application to a four-chamber heart model. Growth models have been applied to HLHS physiology: Dewan et al. (2017) used volumetric growth modeling to investigate the hypothesis that decreased ventricular filling reduces LV growth in utero. Moreover, Del Bianco et al. (2018) have investigated electromechanical changes taking place upon volumetric growth using a univentricle geometry.

Modeling of electrophysiology at organ level necessitates consideration of various aspects such as the fibrous structure, cardiac conduction system, cell electrophysiology models and solving the resulting coupled problem, which are discussed extensively in excellent review articles by Lopez-Perez et al. (2015); Peirlinck et al. (2021b); Corral-Acero et al. (2020); Niederer et al. (2019). In the absence of DT-MRI data, myocardium fibers can be modeled using rule-based methods (Bayer et al. 2012; Bishop et al. 2009).Fast-conducting Purkinje network can be approximated using novel algorithms (Abboud et al. 1991; Costabal et al. 2016), transmembrane potential at cell level can be modeled using phenomenological (FitzHugh 1961; Aliev and Panfilov 1996) or realistic ionic models (Hodgkin and Huxley 1952; Beeler and Reuter 1977; Ten Tusscher and Panfilov 2006). Finally, the coupled conduction and ionic reaction problem of electrophysiology can be solved by means of finite element method (Göktepe and Kuhl 2009), Eikonal approximation (Colli Franzone et al. 1990) or

isogeometric analysis (Pegolotti et al. 2019). Studies using computational electrophysiology modeling in pediatrics are rare in literature; among which are, fetal electrophysiology models (Pervolaraki et al. 2014; Biktasheva et al. 2018) and arrhythmia modeling in pediatric patients (Cartoski et al. 2019; Shade et al. 2020).

We built and calibrated a personalized heart model based on medical imaging and electrocardiographic data of a six-and-a-half-year-old female patient with HLHS. This framework allowed us to systematically study the impact of ventricular growth on electrical dyssynchrony in a controlled manner, examining effects of RV and LV loading-induced growth independently and together. Our study uncovered several important findings:

First, we conclude that the systemic right ventricle in our HLHS patient is highly dyssynchronous, which is line with earlier work by Motonaga et al. (2012). As long QRS is associated with increased risk of arrhythmia, heart failure, and death (Abd El Rahman et al. 2000; Karikari et al. 2020), it is important to assess how loading-induced growth can affect this duration. Our results show that loading-induced right ventricular enlargement leads to a dramatic increase in QRS duration and interventricular dyssynchrony. This effect is purely due to HLHS anatomy; since we assumed a healthy electrical conduction system, normal myofiber structure and healthy material properties. This finding agrees with studies in Tetralogy of Fallot patients where the size of the right ventricle has been associated with QRS elongation (Abd El Rahman et al. 2000). In our simulations, the QRS complex widened approximately 30% (it increased from 70 to 90 ms) as a result of roughly doubling the volume of the right ventricular cavity corresponding to approximately six years of growth. In the literature, the QRS duration in patients with HLHS is observed to increase approximately 12 ms in the six years following the Fontan operation (Khan et al. 2015; Karikari et al. 2020), which is slightly lower than our simulated QRS elongation values. One possible explanation for this discrepancy could be that Purkinje conduction velocities increase with age (Rosen et al. 1981), as a partially compensatory mechanism for QRS elongation. To test this hypothesis, we increased the Purkinje conduction velocities in Table 2 by 20% and recomputed the spatiotemporal activation pattern in the RV + LV loading-induced growth case. This resulted in a smaller QRS elongation of about 10 ms, which agrees more closely with the literature. However, data on conduction velocities in the human heart during childhood are needed before we can draw further conclusions.

Second, we found an inverse relationship between left ventricular enlargement and interventricular dyssynchrony. The activation times of the personalized electrophysiology simulations (Figure 6) show that the left ventricle begins and completes activation earlier than the right ventricle. This observation supports the finding of Monaco et al. (2015) about pre-excited appearance of ECG of HLHS patients. Following the enlargement of the left ventricle, ventricular activation times merge with each other, decreasing interventricular dyssynchrony. This outcome is diminished and reversed when right ventricular enlargement is present along with left ventricular enlargement. This is due to the relative size difference between the left and right ventricle in HLHS patients, before and after growth. Here, the left ventricular hypertrophic wall thickness, and the resulting difference in wall stiffness also play a role in the relative left versus right ventricular loading-induced enlargement. In Section 3.2 we observed that the left ventricle has enlarged approximately 50% and right ventricle enlarged about 100% in response to the same pressure level of 10 mmHg. Hypoplastic left ventricles have endocardial fibroelastosis, which is shown to restrict ventricular capacity and growth (Xu et al. 2015). Although this is a major reason for the stiffness of the ventricle, we observe increased left ventricle stiffness without the presence of fibrosis in our heart model. We conclude that the HLHS geometry with thick left ventricle walls is a contributor to the increased left ventricular stiffness.

Our study has several limitations that need to be noted. First, we defined myofiber orientations using a Laplace-Dirichlet rule based algorithm. Ideally, fiber orientations in the model would be informed by DTMRI data or disease specific measurements. However, such data was not available for this patient and is not routinely collected. Apart from a single myofiber architecture analysis of a one-year-old male patient with a univentricular systemic right ventricle (Tous et al. 2020), data on hallmark transmural fiber orientation in univentricular patients is lacking in the literature. Given the high heterogeneity of the single ventricle patient population, we chose to inform our model based on a healthy myofiber architecture. Given the comparative nature of our study, this limitation about fiber architecture should not affect the overall results, but we note that our model could be updated in future should such data become available, keeping the rest of the modeling pipeline intact. Second, we employed a healthy electrical conduction

system when simulating electrophysiology and tune this to match the personalized electrocardiographic recordings. As the three-stage surgery is confined largely to the atria and outflow tracts, and therefore a significant impact upon the Purkinje system and ventricular conduction is not typically observed, this was felt to be a reasonable assumption given the lack of available data in the HLHS population. In future work, we could expand our framework to incorporate more patient or disease-specific information as it becomes available. In particular, we note that there could be changes in the conduction velocity with age which we have not accounted for due to lack of available data. Third, although we closely matched the patient's grown chamber volumes with our load-induced growth simulations, we did not have the means to compare chamber shapes because the patient did not have an MRI scan available from the given time point (at 11 years 4 months old). We did not account for the prestressed state of the baseline heart geometry (Peirlinck et al. 2018); which could affect the grown geometries slightly. Fourth, this study focused on a female patient. In the future, we aim to expand this study to include both male and female patients, as sex differences in cardiac function cannot be ignored (Peirlinck et al. 2021a; St Pierre et al. 2022). Lastly, a limitation of the proposed discretization is the imposed continuity of voltage at the Purkinje-myocardium junction which ignores possible conduction delays at the Purkinje-myocardium junction (Kamiyama and Inoue 1971). Given the limitations, this study is meant as a pilot study to explore preliminary agreement. More data would be needed to validate this method for clinical use. In future work, we aim to further expand this framework toward electromechanically coupled simulations (Sahli Costabal et al. 2017; Peirlinck et al. 2022) to further elucidate the underlying mechanisms between electrical and mechanical dyssynchrony in this challenging patient population (Motonaga et al. 2012).

Our study has important implications for the future understanding and treatment of patients with HLHS. Most importantly, a better understanding of dyssynchrony in the clinically challenging single ventricle population is key to developing more personalized approaches that can improve the outcomes of patients who required pacing. Our results highlight the importance of taking into account the unique geometrical and loading-induced growth patterns in designing these treatment therapies. Moreover, the developed framework could contribute to novel clinical tools to test and optimize pacing locations, as smaller prior studies have shown that more optimal pacing locations can mitigate the adverse impact of ventricular pacing (Chubb et al. 2022). In parallel, our simulated results of interventricular dyssynchrony show that loading-induced left ventricular enlargement can help restore a more synchronous activation in the Fontan physiology. This is in line with recent clinical efforts to restore biventricular function, albeit in limited patient populations (Emani et al. 2012). We believe that in-silico modeling approaches form a promising future to guide more optimal personalized treatments in the highly heterogeneous univentricular patient population (Chubb et al. 2022).

Disclosure statement

The authors report that there are no competing interests to declare.

Funding

This work was supported by the NSF Grant SI2-SSI 1663671 'The SimCardio open source multi-physics cardiac modeling package' and the NIH Grant R01 HL131823 'A new framework for understanding the mechanisms of diastolic dysfunction'.

References

Abboud S, Berenfeld O, Sadeh D. 1991. Simulation of high-resolution qrs complex using a ventricular model with a fractal conduction system. Effects of ischemia on high-frequency QRS potentials. Circ Res. 68(6):1751–1760.

Abd El Rahman M, Abdul-Khaliq H, Vogel M, Alexi-Meskishvili V, Gutberlet M, Lange P. 2000. Relation between right ventricular enlargement, qrs duration, and right ventricular function in patients with tetralogy of fallot and pulmonary regurgitation after surgical repair. Heart. 84(4):416–420.

Aliev RR, Panfilov AV. 1996. A simple two-variable model of cardiac excitation. Chaos Soliton Fract. 7(3):293–301.

Barber F, Langfield P, Lozano M, García-Fernández I, Duchateau J, Hocini M, Haïssaguerre M, Vigmond E, Sebastian R. 2021. Estimation of personalized minimal purkinje systems from human electro-anatomical maps. IEEE Trans Med Imaging. 40(8):2182–2194.

Bayer JD, Blake RC, Plank G, Trayanova NA. 2012. A novel rule-based algorithm for assigning myocardial fiber orientation to computational heart models. Ann Biomed Eng. 40(10):2243–2254.

Beeler GW, Reuter H. 1977. Reconstruction of the action potential of ventricular myocardial fibres. J Physiol. 268(1):177–210.

Biktasheva IV, Anderson RA, Holden AV, Pervolaraki E, Wen FC. 2018. Cardiac re-entry dynamics and self-termination in dt-MRI based model of human fetal heart. Front Phys. 6:15.

Bishop MJ, Hales P, Plank G, Gavaghan DJ, Scheider J, Grau V. 2009. Comparison of rule-based and dtmri-derived fibre architecture in a whole rat ventricular computational model. In: Functional Imaging and Modeling of the Heart: 5th International Conference, FIMH 2009; June 3–5, 2009; Nice, France: Springer. p. 87–96.

Cartoski MJ, Nikolov PP, Prakosa A, Boyle PM, Spevak PJ, Trayanova NA. 2019. Computational identification of ventricular arrhythmia risk in pediatric myocarditis. Pediatr Cardiol. 40(4):857–864.

Chubb H, Bulic A, Mah D, Moore JP, Janousek J, Fumanelli J, Asaki SY, Pflaumer A, Hill AC, Escudero C, et al. 2022. Impact and modifiers of ventricular pacing in patients with single ventricle circulation. J Am Coll Cardiol. 80(9):902–914.

Colli Franzone P, Guerri L, Rovida S. 1990. Wavefront propagation in an activation model of the anisotropic cardiac tissue: asymptotic analysis and numerical simulations. J Math Biol. 28(2):121–176.

Corral-Acero J, Margara F, Marciniak M, Rodero C, Loncaric F, Feng Y, Gilbert A, Fernandes JF, Bukhari HA, Wajdan A, et al. 2020. The 'digital twin'to enable the vision of precision cardiology. Eur Heart J. 41(48): 4556–4564.

Costabal FS, Hurtado DE, Kuhl E. 2016. Generating purkinje networks in the human heart. J Biomech. 49(12): 2455–2465.

Dassault Systèmes Simulia Corp. 2022. Abaqus analysis user's guide.

Del Bianco F, Franzone PC, Scacchi S, Fassina L. 2018. Electromechanical effects of concentric hypertrophy on the left ventricle: a simulation study. Comput Biol Med. 99:236–256.

Dewan S, Krishnamurthy A, Kole D, Conca G, Kerckhoffs R, Puchalski MD, Omens JH, Sun H, Nigam V, McCulloch AD. 2017. Model of human fetal growth in hypoplastic left heart syndrome: reduced ventricular growth due to decreased ventricular filling and altered shape. Front Pediatr. 5:25.

Durrer D, Van Dam RT, Freud G, Janse M, Meijler F, Arzbaecher R. 1970. Total excitation of the isolated human heart. Circulation. 41(6):899–912.

Emani SM, McElhinney DB, Tworetzky W, Myers PO, Schroeder B, Zurakowski D, Pigula FA, Marx GR, Lock JE, del Nido PJ. 2012. Staged left ventricular recruitment after single-ventricle palliation in patients with borderline left heart hypoplasia. J Am Coll Cardiol. 60(19):1966–1974.

Files MD, Arya B. 2018. Pathophysiology, adaptation, and imaging of the right ventricle in fontan circulation. Am J Physiol Heart Circ Physiol. 315(6):H1779–H1788.

FitzHugh R. 1961. Impulses and physiological states in theoretical models of nerve membrane. Biophys J. 1(6):445–466.

Fontan F, Baudet E. 1971. Surgical repair of tricuspid atresia. Thorax. 26(3):240–248.

Genet M, Lee LC, Baillargeon B, Guccione JM, Kuhl E. 2016. Modeling pathologies of diastolic and systolic heart failure. Ann Biomed Eng. 44(1):112–127.

Geuzaine C, Remacle JF. 2009. Gmsh: a 3-D finite element mesh generator with built-in pre-and post-processing facilities. Int J Numer Meth Engng. 79(11):1309–1331.

Gillette K, Prassl A, Neic A, Plank G, Bayer J, Vigmond E. 2018. Automatic generation of bi-ventricular models of cardiac electrophysiology for patient specific personalization using non-invasive recordings. Vol. 45. In 2018 computing in cardiology conference (CinC). IEEE; p. 1–4.

Gobergs R, Salputra E, Lubaua I. 2016. Hypoplastic left heart syndrome: a review. Acta Med Litu. 23(2):86–98.

Göktepe S, Abilez OJ, Kuhl E. 2010a. A generic approach towards finite growth with examples of athlete's heart, cardiac dilation, and cardiac wall thickening. J Mech Phys Solids. 58(10):1661–1680.

Göktepe S, Abilez OJ, Parker KK, Kuhl E. 2010b. A multiscale model for eccentric and concentric cardiac growth through sarcomerogenesis. J Theor Biol. 265(3):433–442.

Göktepe S, Kuhl E. 2009. Computational modeling of cardiac electrophysiology: a novel finite element approach. Int J Numer Meth Engng. 79(2):156–178.

Graham EM, Scheurer MA, Saul J P, Bradley SM, Atz AM. 2007. QRS duration following the norwood procedure: blalock-taussig shunt versus right ventricle to pulmonary artery shunt. Pacing Clin Electrophysiol. 30(11):1336–1338.

Grattan M, Mertens L. 2016. Mechanics of the functionally univentricular heart—how little do we understand and why does it matter? Can J Cardiol. 32(8):1033.e11–1033–e18.

Gutgesell HP, Massaro TA. 1995. Management of hypoplastic left heart syndrome in a consortium of university hospitals. Am J Cardiol. 76(11):809–811.

Hayama Y, Shimizu S, Kawada T, Negishi J, Sakaguchi H, Miyazaki A, Ohuchi H, Yamada O, Kurosaki K, Sugimachi M. 2020. Impact of delayed ventricular wall area ratio on pathophysiology of mechanical dyssynchrony: implication from single-ventricle physiology and 0d modeling. J Physiol Sci. 70(1):1–13.

Hodgkin AL, Huxley AF. 1952. A quantitative description of membrane current and its application to conduction and excitation in nerve. J Physiol. 117(4):500–544.

Holzapfel GA, Ogden RW. 2009. Constitutive modelling of passive myocardium: a structurally based framework for material characterization. Philos Trans A Math Phys Eng Sci. 367(1902):3445–3475.

Joyce J, O'Leary ET, Mah DY, Harrild DM, Rhodes J. 2020. Cardiac resynchronization therapy improves the ventricular function of patients with fontan physiology. Am Heart J. 230:82–92.

Kamiyama A, Inoue F. 1971. Conduction delay from purkinje fiber to ventricular muscle studied with extracellular microelectrodes. Can J Physiol Pharmacol. 49(7):678–684.

Karikari Y, Abdulkarim M, Li Y, Loomba RS, Zimmerman F, Husayni T. 2020. The progress and significance of qrs duration by electrocardiography in hypoplastic left heart syndrome. Pediatr Cardiol. 41(1):141–148.

Khan S, Nadorlik H, Kertesz N, Nicholson L, Ro PS, Cua CL. 2015. QRS duration changes in patients with single ventricle physiology: birth to 10 years. Pacing Clin Electrophysiol. 38(10):1159–1165.

Klotz S, Hay I, Dickstein ML, Yi GH, Wang J, Maurer MS, Kass DA, Burkhoff D. 2006. Single-beat estimation of end-diastolic pressure-volume relationship: a novel

method with potential for noninvasive application. Am J Physiol Heart Circ Physiol. 291(1):H403–H412.
Krishnamoorthi S, Sarkar M, Klug WS. 2013. Numerical quadrature and operator splitting in finite element methods for cardiac electrophysiology. Int J Numer Method Biomed Eng. 29(11):1243–1266.
Kroon W, Delhaas T, Arts T, Bovendeerd P. 2009. Computational modeling of volumetric soft tissue growth: application to the cardiac left ventricle. Biomech Model Mechanobiol. 8(4):301–309.
Lee AW, Costa CM, Strocchi M, Rinaldi CA, Niederer SA. 2018. Computational modeling for cardiac resynchronization therapy. J Cardiovasc Transl Res. 11(2):92–108.
Lin IE, Taber L. 1995. A model for stress-induced growth in the developing heart.
Lopez L, Cohen MS, Anderson RH, Redington AN, Nykanen DG, Penny DJ, Deanfield JE, Eidem BW. 2010. Unnatural history of the right ventricle in patients with congenitally malformed hearts. Cardiol Young. 20(S3): 107–112.
Lopez-Perez A, Sebastian R, Ferrero JM. 2015. Three-dimensional cardiac computational modelling: methods, features and applications. BioMed Eng OnLine. 14(1):31.
Marsden AL, Feinstein JA. 2015. Computational modeling and engineering in pediatric and congenital heart disease. Curr Opin Pediatr. 27(5):587–596.
McEvoy E, Holzapfel GA, McGarry P. 2018. Compressibility and anisotropy of the ventricular myocardium: experimental analysis and microstructural modeling. J Biomech Eng. 140(8):081004.
Monaco MA, Liberman L, Starc TJ, Silver ES. 2015. Defining the electrocardiogram in the neonate with hypoplastic left heart syndrome. Pediatr Cardiol. 36(5): 1014–1018.
Motonaga KS, Miyake CY, Punn R, Rosenthal DN, Dubin AM. 2012. Insights into dyssynchrony in hypoplastic left heart syndrome. Heart Rhythm. 9(12):2010–2015.
Niederer SA, Kerfoot E, Benson AP, Bernabeu MO, Bernus O, Bradley C, Cherry EM, Clayton R, Fenton FH, Garny A, et al. 2011. Verification of cardiac tissue electrophysiology simulators using an n-version benchmark. Philos Trans A Math Phys Eng Sci. 369(1954):4331–4351.
Niederer SA, Lumens J, Trayanova NA. 2019. Computational models in cardiology. Nat Rev Cardiol. 16(2):100–111.
Niestrawska JA, Augustin CM, Plank G. 2020. Computational modeling of cardiac growth and remodeling in pressure overloaded hearts–linking microstructure to organ phenotype. Acta Biomater. 106:34–53.
Noonan JA, Nadas AS. 1958. The hypoplastic left heart syndrome. Pediatr Clin North Am. 5(4):1029–1056.
O'Hara T, Virág L, Varró A, Rudy Y. 2011. Simulation of the undiseased human cardiac ventricular action potential: model formulation and experimental validation. PLoS Comput Biol. 7(5):e1002061.
Ohye RG, Schranz D, D'Udekem Y. 2016. Current therapy for hypoplastic left heart syndrome and related single ventricle lesions. Circulation. 134(17):1265–1279.
Pegolotti L, Dedè L, Quarteroni A. 2019. Isogeometric analysis of the electrophysiology in the human heart: numerical simulation of the bidomain equations on the atria. Comp Methods Appl Mech Eng. 343:52–73.
Peirlinck M, Beule MD, Segers P, Rebelo N. 2018. A modular inverse elastostatics approach to resolve the pressure-induced stress state for in vivo imaging based cardiovascular modeling. J Mech Behav Biomed Mater. 85:124–133.
Peirlinck M, Costabal FS, Kuhl E. 2021a. Sex differences in drug-induced arrhythmogenesis. Front Physiol. 12:1245.
Peirlinck M, Costabal FS, Sack KL, Choy JS, Kassab GS, Guccione JM, Beule MD, Segers P, Kuhl E. 2019a. Using machine learning to characterize heart failure across the scales. Biomech Model Mechanobiol. 18(6):1987–2001.
Peirlinck M, Costabal FS, Yao J, Guccione JM, Tripathy S, Wang Y, Ozturk D, Segars P, Morrison TM, Levine S, et al. 2021b. Precision medicine in human heart modeling: perspectives, challenges, and opportunities. Biomech Model Mechanobiol. 20(3):803–831.
Peirlinck M, Costabal FS, Yao J, Guccione JM, Tripathy S, Wang Y, Ozturk D, Segars P, Morrison TM, Levine S, et al. 2021c. Precision medicine in human heart modeling. Biomech Model Mechanobiol. 20(3):803–831.
Peirlinck M, Sack KL, De Backer P, Morais P, Segers P, Franz T, De Beule M. 2019b. Kinematic boundary conditions substantially impact in silico ventricular function. Int J Numer Method Biomed Eng. 35(1):e3151.
Peirlinck M, Yao J, Costabal FS, Kuhl E. 2022. How drugs modulate the performance of the human heart. Comput Mech. 69(6):1397–1411.
Ferencz C, Rubin JD, Mccarter RJ, Brenner JI, Neill CA, Perry LW, Hepner SI, Downing JW. 1985. Congenital heart disease: prevalence at livebirth: the Baltimore-Washington Infant Study. American journal of epidemiology. 121(1):31–36.
Pervolaraki E, Hodgson S, Holden AV, Benson AP. 2014. Towards computational modelling of the human foetal electrocardiogram: normal sinus rhythm and congenital heart block. Europace. 16(5):758–765.
Pezzuto S, Hake J, Sundnes J. 2016. Space-discretization error analysis and stabilization schemes for conduction velocity in cardiac electrophysiology. Int J Numer Meth Biomed Engng. 32(10):e02762.
Qu Z, Garfinkel A. 1999. An advanced algorithm for solving partial differential equation in cardiac conduction. IEEE Trans Biomed Eng. 46(9):1166–1168.
Ramasubramanian A, Nerurkar NL, Achtien KH, Filas BA, Voronov DA, Taber LA. 2008. On modeling morphogenesis of the looping heart following mechanical perturbations. J Biomech Eng. 130(6):061018.
Rathod RH, Prakash A, Kim YY, Germanakis IE, Powell AJ, Gauvreau K, Geva T. 2014. Cardiac magnetic resonance parameters predict transplantation-free survival in patients with fontan circulation. Circ. Cardiovas Imaging. 7(3):502–509.
Rodriguez EK, Hoger A, McCulloch AD. 1994. Stress-dependent finite growth in soft elastic tissues. J Biomech. 27(4):455–467.
Rohmer D, Sitek A, Gullberg GT. 2007. Reconstruction and visualization of fiber and laminar structure in the normal human heart from ex vivo diffusion tensor magnetic resonance imaging (DTMRI) data. Invest Radiol. 42(11): 777–789.

Rosen MR, Legato MJ, Weiss RM. 1981. Developmental changes in impulse conduction in the canine heart. Am J Physiol. 240(4):H546–H554.
Rösner A, Khalapyan T, Dalen H, McElhinney DB, Friedberg MK, Lui GK. 2018. Classic-pattern dyssynchrony in adolescents and adults with a fontan circulation. J Am Soc Echocardiogr. 31(2):211–219.
Sahli Costabal F, Concha FA, Hurtado DE, Kuhl E. 2017. The importance of mechano-electrical feedback and inertia in cardiac electromechanics. Comput Methods Appl Mech Eng. 320:352–368.
Sahli Costabal F, Yao J, Kuhl E. 2018. Predicting the cardiac toxicity of drugs using a novel multiscale exposure–response simulator. Comput Methods Biomech Biomed Engin. 21(3):232–246.
Salman HE, Yalcin HC. 2021. Computational modeling of blood flow hemodynamics for biomechanical investigation of cardiac development and disease. JCDD. 8(2):14.
Schwarz EL, Kelly JM, Blum KM, Hor KN, Yates AR, Zbinden JC, Verma A, Lindsey SE, Ramachandra AB, Szafron JM, et al. 2021. Hemodynamic performance of tissue-engineered vascular grafts in fontan patients. NPJ Regener Med. 6(1):1–17.
Shade JK, Cartoski MJ, Nikolov P, Prakosa A, Doshi A, Binka E, Olivieri L, Boyle PM, Spevak PJ, Trayanova NA. 2020. Ventricular arrhythmia risk prediction in repaired tetralogy of fallot using personalized computational cardiac models. Heart Rhythm. 17(3):408–414.
Sharifi H, Mann CK, Rockward AL, Mehri M, Mojumder J, Lee LC, Campbell KS, Wenk JF. 2021. Multiscale simulations of left ventricular growth and remodeling. Biophys Rev. 13(5):729–746.
Sobh M, Freitag-Wolf S, Scheewe J, Kanngiesser LM, Uebing AS, Gabbert DD, Voges I. 2022. Serial right ventricular assessment in patients with hypoplastic left heart syndrome: a multiparametric cardiovascular magnetic resonance study. Eur J Cardiothorac Surg. 61(1):36–42.
Sommer G, Schriefl AJ, Andrä M, Sacherer M, Viertler C, Wolinski H, Holzapfel GA. 2015. Biomechanical properties and microstructure of human ventricular myocardium. Acta Biomater. 24:172–192.
St Pierre SR, Peirlinck M, Kuhl E. 2022. Sex matters: a comprehensive comparison of female and male hearts. Front Physiol. 13:831179.
Sughimoto K, Ueda T, Fujiwara T, Liu H. 2019. Impact of atrial fibrillation on hemodynamics of fontan circulation: fontan computational model study. Circulation. 140(Suppl_1):A12557–A12557.
Sundareswaran KS, Pekkan K, Dasi LP, Whitehead K, Sharma S, Kanter KR, Fogel MA, Yoganathan AP. 2008. The total cavopulmonary connection resistance: a significant impact on single ventricle hemodynamics at rest and exercise. Am J Physiol Heart Circ Physiol. 295(6):H2427–H2435.
Taber L, Chabert S. 2002. Theoretical and experimental study of growth and remodeling in the developing heart. Biomech Model Mechanobiol. 1(1):29–43.
Ten Tusscher K, Panfilov AV. 2008. Modelling of the ventricular conduction system. Prog Biophys Mol Biol. 96(1–3):152–170.
Ten Tusscher KH, Panfilov AV. 2006. Alternans and spiral breakup in a human ventricular tissue model. Am J Physiol Heart Circ Physiol. 291(3):H1088–H1100.
Tous C, Gentles TL, Young AA, Pontré BP. 2020. Ex vivo cardiovascular magnetic resonance diffusion weighted imaging in congenital heart disease, an insight into the microstructures of tetralogy of fallot, biventricular and univentricular systemic right ventricle. J Cardiovasc Magn Reson. 22(1):1–12.
Trusty PM, Slesnick TC, Wei ZA, Rossignac J, Kanter KR, Fogel MA, Yoganathan AP. 2018. Fontan surgical planning: previous accomplishments, current challenges, and future directions. J Cardiovasc Transl Res. 11(2):133–144.
Tsai S, Husain N, Fischer A, Ro PS, Cheatham JP, Galantowicz M, Cua CL. 2013. QRS duration changes in patients with hypoplastic left heart syndrome undergoing hybrid palliation: prehybrid to post-fontan. Pacing Clin Electrophysiol. 36(4):462–466.
Updegrove A, Wilson NM, Merkow J, Lan H, Marsden AL, Shadden SC. 2017. Simvascular: an open source pipeline for cardiovascular simulation. Ann Biomed Eng. 45(3):525–541.
Virtanen P, Gommers R, Oliphant TE, Haberland M, Reddy T, Cournapeau D, Burovski E, Peterson P, Weckesser W, Bright J, et al. 2020. SciPy 1.0: fundamental Algorithms for scientific computing in Python. Nat Methods. 17(3):261–272.
Wen Zhong S, Zhang YQ, Jun Chen L, Zhang ZF, Wu LP, Jing Hong W. 2021. Ventricular function and dyssynchrony in children with a functional single right ventricle using real time three-dimensional echocardiography after fontan operation. Echocardiography. 38(8):1218–1227.
Woodworth LA, Cansız B, Kaliske M. 2022. Balancing conduction velocity error in cardiac electrophysiology using a modified quadrature approach. Numer Methods Biomed Eng. 38(5):e3589.
Wünnemann F, Andelfinger GU. 2016. Molecular pathways and animal models of hypoplastic left heart syndrome. In: Congenital heart diseases: the broken heart. Vienna: Springer; p. 649–664.
Xu X, Friehs I, Zhong Hu T, Melnychenko I, Tampe B, Alnour F, Iascone M, Kalluri R, Zeisberg M, Del Nido PJ, et al. 2015. Endocardial fibroelastosis is caused by aberrant endothelial to mesenchymal transition. Circ Res. 116(5):857–866.
Yang W, Chan FP, Reddy VM, Marsden AL, Feinstein JA. 2015. Flow simulations and validation for the first cohort of patients undergoing the y-graft fontan procedure. J Thorac Cardiovasc Surg. 149(1):247–255.
Zaidi SJ, Penk J, Cui VW, Roberson DA. 2019. Right ventricular mechanical dyssynchrony in hypoplastic left heart syndrome: correlation with systolic function and qrs duration. Pediatr Cardiol. 40(5):934–942.

Appendix A.

Verification of the electrophysiology solver

Electrophysiology problem with complex ionic models does not permit an analytical solution that could be used to validate numerical solutions. Therefore, in Niederer

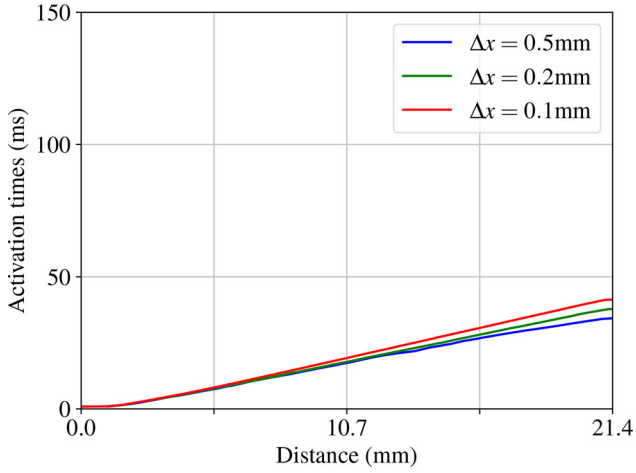

Figure A1. Activation times along the diagonal line depicted in Figure 1(b) of Niederer et al. (2011) between points $P1 = (0, 0, 0)$ and $P8 = (20, 7, 3)$ of the solution domain, for solutions with $\Delta t = 0.005$ ms and $\Delta x = 0.1$ mm (red line), $\Delta x = 0.2$ mm (green line) and $\Delta x = 0.5$ mm (blue line).

et al. (2011) authors have proposed an example problem that could serve for this purpose. Nine research groups have presented their numerical solutions to this example problem using a range of solution techniques. This problem considers excitation of a representative tissue piece in shape of a rectangular slab with dimensions of 20mm × 7mm × 3mm. The slab was excited at the corner (0, 0, 0) and activation was observed along the diagonal line connecting the corners (0, 0, 0) and (20, 7, 3). The problem setting dictates the use of the Ten Tusscher-Panfilov model Ten Tusscher and Panfilov (2006) with modified parameters.

Table A1. Activation times at the corner (20mm, 7mm, 3mm), for combinations of time and space discretizations.

	$\Delta x = 0.1$ mm	$\Delta x = 0.2$ mm	$\Delta x = 0.5$ mm
$\Delta t = 0.05$ ms	43.88 ms	39.85 ms	35.78 ms
$\Delta t = 0.01$ ms	41.83 ms	37.92 ms	34.41 ms
$\Delta t = 0.005$ ms	41.37 ms	37.84 ms	34.32 ms

Nine research groups have submitted their solutions to the example problem and authors have concluded the correct solution to the activation of the point (20mm, 7mm, 3mm) should be between 42.5 ms to 43.0 ms, however, it should be noted that only two out of nine of the solutions fell into this range. Our solution of the problem resulted in an activation time of 41.37 ms using the finest time and space discretizations (see Table A1 and Figure A1). We note that we used central quadrature in solving the diffusion problem (see Figure 2, left). We observed an early activation, indicating increased conduction velocity, with coarser space discretization. This behavior can be modified by choosing different quadrature locations as explained in Section 2.6.